Pečenko *et al. Int J Concr Struct Mater* (2019) 13:60
https://doi.org/10.1186/s40069-019-0373-9

International Journal of Concrete Structures and Materials

RESEARCH Open Access

A Computational Model for Prestressed Concrete Hollow-Core Slab Under Natural Fire

R. Pečenko*, T. Hozjan, I. Planinc and S. Bratina

Abstract

Performance-based approach, introducing a new two-phase computational model for determining the response of prestressed hollow-core concrete slab exposed to natural fire including heating and cooling phase, is presented. Firstly, the two-dimensional coupled hygro-thermo-chemical model is used to determine time dependent temperature and moisture field in the characteristic cross-section of the concrete hollow-core slab during fire. In addition, the influence of opening on the temperature distribution over prestressed hollow-core concrete slab is accounted for. Secondly, stress–strain state of prestressed concrete hollow-core slab is determined with a newly developed one-dimensional geometrical and material non-linear model, which includes a slip between concrete and tendon. Temperature dependent mechanical properties of concrete, tendon and bond stiffness are accounted for in the model. Model validation showed that the presented two-phase computational model is suitable for the analysis of prestressed hollow-core concrete slab exposed to natural fire. Furthermore, parametric studies revealed that heat exchange between the concrete section and the opening has a significant influence on the development of temperatures in the slab, particularly in the cooling phase, and consequently also on the development of slab displacements. In addition, it was identified that accounting for the slip between concrete and tendon enables the determination of the bond stress distribution and evaluation of the load bearing capacity of the contact.

Keywords: prestressed hollow-core concrete slab, natural fire, bond stress-slip, hygro-thermo-chemical analysis, mechanical analysis, FEM

1 Introduction

Prestressed hollow-core concrete slab (hereinafter HC slab) is known as one of the most frequently built-in precast concrete elements nowadays. Among the many advantages offered by the HC slab there is also a favorable behaviour during fire (Bailey and Lennon 2008; Aguado et al. 2012; Park et al. 2019). However, precise determination of the fire behaviour of the HC slab is far from trivial, meaning that it is necessary to understand the physical and chemical phenomena that govern the behaviour of the slab.

At elevated temperatures, different chemical and physical processes occur in concrete (Tufail et al. 2017). Being a hygroscopic and porous material, the transfer of moisture has an important influence on the temperature distribution within concrete during fire (Davie et al. 2006; Hozjan et al. 2010; Kolšek et al. 2014). Therefore, heat and moisture transfer needs to be treated as a coupled problem. In addition, the dehydration of chemically bound water also effects the temperature field, therefore chemical processes need to be coupled to the heat and moisture transfer as well. Furthermore, concrete is subjected to extensive creep and material degradation at elevated temperatures, which results in reduced load bearing capacity of the HC slab. The behaviour of prestressing steel at elevated temperatures has even greater influence on the behaviour of the HC slab in fire. Namely, strength and stiffness properties of prestressing steel significantly deteriorate with temperature increase, especially for the temperatures above 400 °C, where, in addition, viscous creep of steel occurs, resulting in significant loss of mechanical properties of prestressing steel, followed by the increased deformability and reduced fire resistance

*Correspondence: robert.pecenko@fgg.uni-lj.si
Faculty of Civil and Geodetic Engineering, University of Ljubljana, Jamova 2, 1115 Ljubljana, Slovenia
ISSN 1976-0485 / eISSN 2234-1315.

and possible failure of the HC slab (Bratina et al. 2003; Wei et al. 2016). Besides that, bond degradation between concrete and prestressing tendon at elevated temperatures can also have significant influence on the HC slab behaviour during fire.

Although the performance of the HC slab in fire is driven by different complex phenomena, the traditional engineering practice to determine fire resistance of the HC slab still follows tabulated data that can be provided by the manufacturers or found in simple design methods such as given in CEN (2005). An essential drawback of these methods is that they are based on the standard ISO fire exposure. However, it is well known that the fire behaviour is highly uncertain phenomenon and the ISO curve cannot describe all the possible fire scenarios. In addition, when applying tabulated data or simple design methods, the behaviour of the HC slab during fire is not known and the estimation of post fire capacity is impossible. To overcome the described drawbacks, an advanced approach has to be introduced, called performance-based approach, which is based on the use of advanced numerical models to describe the behaviour of the HC slab in fire.

Recently developed numerical models for the simulation of the behaviour of the HC slabs during fire can be found in (Aguado et al. 2016; Ellobody 2014; Shakya and Kodur 2015; Kodur and Shakya 2014; Min et al. 2010; Chang et al. 2008; Shakya and Kodur 2017; Khalaf and Huang 2016). Although these models represent state-of-the-art in this field, they still lack the description of some important physical phenomena, with certain simplifications taken into account. Namely, in all models simplified thermal analysis was performed based on the Fourier partial differential equation, describing the heat transfer through solid body, thus neglecting the influence of moisture transfer on temperature distribution, pressure increase in concrete pores, dehydration of chemically bound water and many others. Further on, the influence of creep and transient strain of concrete at elevated temperatures was neglected. What is more, in most models (Aguado et al. 2016; Ellobody 2014; Shakya and Kodur 2015; Kodur and Shakya 2014; Min et al. 2010; Chang et al. 2008; Shakya and Kodur 2017) rigid contact between concrete and tendon was considered, while in other models where slip was accounted for (Khalaf and Huang 2016; Ellobody 2014), the intake mechanism and transmission length of the prestressing force as well as the possible failure of the contact at elevated temperatures were not directly addressed. Due to the described simplifications in the models, some discrepancies were observed when validating the results of these models against experimental results. In addition, only the response of the HC slab exposed to standard fire was investigated, thus, potential failure and other phenomena occurring in the cooling phase were not investigated.

Therefore, the main objective of this paper is to present a new developed two-phase numerical model based on the precise physical description of the phenomena occurring in the HC slab during natural fire, thus providing more accurate determination of fire resistance and response of the HC slab exposed to fire for both heating and cooling phase. In order to consider the influence of moisture transfer and dehydration of chemically bound water on the behaviour of the HC slab in fire, own developed coupled hygro-thermo-chemical model (Hozjan et al. 2010; Kolšek et al. 2014), adopted from Davie et al. (2006), is used in the first phase of the numerical model, where, in addition, the influence of the opening within the HC slab geometry on temperature distribution is considered. In the second phase, the newly developed mechanical model to determine the behaviour of the HC slab simultaneously exposed to fire and mechanical load is given. The formulation of the mechanical model is based on the detailed physical description of the problem, where different strain increments are introduced. Even more important, slip at the contact between concrete and tendon is considered, allowing to identify possible failure mechanism of the contact, which has not been addressed so far.

Below, the basic equations of the new numerical model are presented first. In the section numerical solution, novelties and main features of numerical models are emphasized. In the last section numerical example, model validation and parametric studies are given.

2 Basic Equations

Basic equations for the analysis of the HC slab subjected to fire are written separately for the hygro-thermo-chemical analysis and mechanical analysis. The coupling between both phases is performed in a weak manner, i.e. through computational procedure, where the results from the hygro-thermo-chemical analysis are used as an input data for the mechanical analysis. In case of fire, the HC slab is usually in the hot zone, meaning that air temperature along the HC slab does not change significantly. This implies that temperature and moisture field does not change along the HC slab and hygro-thermo-chemical analysis can be determined over a characteristic cross-section of the HC slab. Therefore, basic equations of hygro-thermo-chemical model are written for the 2D domain (Fig. 1). The considered precast element is characterized as a slab, although, in principle, it behaves as a beam element, since load is transmitted to the support only in the longitudinal direction. For this reason, basic equations describing mechanical model are formed on the 1D beam theory.

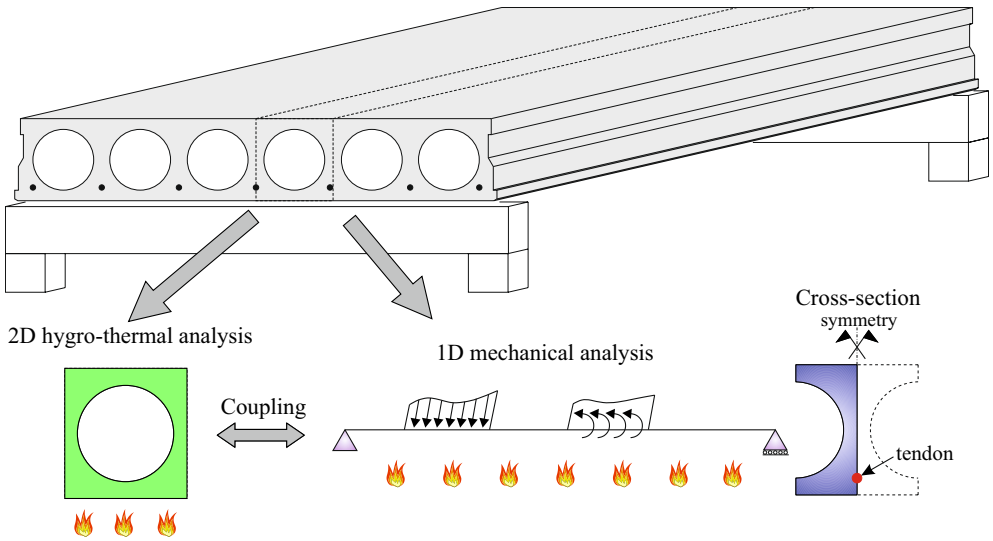

Fig. 1 Modelling of the HC slab.

2.1 Basic Equations of Coupled Hygro-Thermo-Chemical Model

Numerical model for coupled hygro-thermo-chemical analysis is based on the model of Davie et al. (2006) with modifications given in Kolšek et al. (2014). The model is suitable for the 2D hygro-thermo-chemical analysis across the concrete beam cross-section, where the influence of tendon on the distribution of temperatures within the cross-section is neglected. Further on, the model takes into account the evaporation of free water, the liquefaction of water vapour and the dehydration of chemically bond water. In addition, the capillary pressure and the part of the free water co-existing in an absorbed state is also taken into account. The model is described by the system of mass conservation equations for each phase separately and by the energy conservation equation.

Water conservation:

$$\frac{\partial(\varepsilon_{FW}\rho_{FW})}{\partial t} = -\nabla\cdot\mathbf{J}_{FW} - \dot{E}_{FW} + \frac{\partial(\varepsilon_{D}\rho_{FW})}{\partial t}, \quad (1)$$

water vapour conservation:

$$\frac{\partial(\varepsilon_{G}\tilde{\rho}_{V})}{\partial t} = -\nabla\cdot\mathbf{J}_{V} + \dot{E}_{FW}, \quad (2)$$

air conservation:

$$\frac{\partial(\varepsilon_{G}\tilde{\rho}_{A})}{\partial t} = -\nabla\cdot\mathbf{J}_{A}, \quad (3)$$

energy conservation:

$$(\underline{\rho C})\frac{\partial T}{\partial t} = -\nabla\cdot(-k\nabla T) - (\underline{\rho C}\mathbf{v})\cdot\nabla T - \lambda_{E}\dot{E}_{FW} - \lambda_{D}\frac{\partial(\varepsilon_{D}\rho_{FW})}{\partial t}. \quad (4)$$

In Eqs. (1–4) ρ_{FW}, $\tilde{\rho}_{V}$ and $\tilde{\rho}_{A}$ is the mass of free water, water vapour and dry air per unit volume of gaseous mixture. $\varepsilon_{G}\tilde{\rho}_{A}$, $\varepsilon_{G}\tilde{\rho}_{V}$ and $\varepsilon_{FW}\rho_{FW}$ denotes the mass of air, water vapour and free water per unit volume of concrete. $\mathbf{J}_{i}$ refers to the mass flux of phase i ($i = FW, V, A$), $\dot{E}_{FW}$ is the rate of evaporation of free water (desorption included), t is time and ∇ is nabla operator. Furthermore, k and $\underline{\rho C}$ are conductivity and heat capacity of concrete, $\underline{\rho C}\mathbf{v}$ is energy transferred by the fluid flow, λ_{E} and λ_{D} are the specific heat of evaporation and dehydration, $\varepsilon_{D}\rho_{FW}$ is the mass of bound water released by dehydration per unit volume of concrete, and T is the temperature.

By summing Eqs. (1) and (2) three partial differential equations are obtained describing the transfer of dry air, moisture and energy conservation. This three partial differential equations are the rearranged so that the basic unknowns of heat and moisture transfer problem are temperature T, pore pressure P_{G} and water vapour content $\tilde{\rho}_{V}$ (Kolšek et al. 2014). Temperature variation of thermal properties of concrete, air and water vapour are taken according to CEN (2005) and Davie et al. (2006).

The cooling phase of fire is also addressed in the paper. Therefore, certain assumptions are introduced in order to describe the behaviour of concrete in cooling phase. First of all, when chemically bond water is adsorbed into capillary pores it can no longer return to the previous state, i.e. dehydration of chemically bond water is irreversible process and thus simply neglected in the cooling phase. In addition, it is assumed that porosity and permeability of concrete does not change in the cooling phase and are determined at the maximum temperature in each point of concrete section.

Similarly it is applied, that thermal properties of concrete remain constant in the cooling phase and are equal to the values reached at the maximum temperature in each point of the cross-section.

In order to account for the heat and mass exchange between concrete body and the surrounding, the boundary conditions at the boundary layer are prescribed. The heat surface flux at the boundary is given as:

$$\mathbf{n} \cdot \nabla T = \frac{h_{qr}}{k}(T_\infty - T) \tag{5}$$

where $\mathbf{n}$ is normal unit vector of the boundary surface, T_∞ is the surrounding temperature and h_{qr} is the heat transfer coefficient composed of convective part h_q and radiative part h_r. The mass transfer at the boundary is determined as:

$$\mathbf{n} \cdot \mathbf{J}_V = -\beta(\tilde{\rho}_{V,\infty} - \tilde{\rho}_V) \tag{6}$$

where $\tilde{\rho}_{V,\infty}$ is the concentration of water vapour in the surrounding and β is mass transfer coefficient determined in Cengel (1998). Further on, it is assumed that the pressure in concrete pores at the boundary is equal to the environmental pressure $P_{G,\infty}$, hence:

$$P_G = P_{G,\infty} \tag{7}$$

2.1.1 Air, Temperature and Moisture Exchange in the Opening

When analysing the HC slab, the opening in the geometry has an influence on the temperature and moisture distribution within the HC slab. For this reason, the cross-section is divided on two subsections, first is represented by the concrete part and second represents the air within the opening. The exchange of heat through the contact boundary layer of these two subsystems, is formally expressed by the heat flux density. In general, both radiative and convective heat transfer has to be considered. However, simplification is introduced, assuming only convective heat exchange between the body and the opening. In view, the heat flux density between the two subsections.

$$q_B = h_{q,B}(T_B - T_{op}), \tag{8}$$

where T_B denotes temperature of the boundary surface, T_{op} is the air temperate inside the opening and $h_{q,B}$ is the convective coefficient at the boundary surface. Assuming the uniform air temperature inside the opening, the heat flux through the boundary surface size of $1 \times ds$, can be written as:

$$dQ_B = h_{q,B}(T_B - T_{op})ds. \tag{9}$$

where ds denotes the partial arc-length of the boundary surface. The entire heat flux at the contact between the two subsystems can be obtained by integrating heat flux density along internal edge of opening:

$$Q_B = \int_0^{L_{op}} h_{q,B} T_B ds - T_{op} \int_0^{L_{op}} h_{q,B} ds, \tag{10}$$

where L_{op} denotes the perimeter of the opening. The internal energy of the air is dependent on the air mass m, specific heat at constant volume c_v and on the change of air temperature dT_{op} within the opening.

$$Q_B dt = m c_v dT_{op}. \tag{11}$$

Air mass can be expressed as product of air density ρ_A and total air volume V_A within the opening. After the arrangement the heat flux can be written as:

$$Q_B = \rho_A V_A c_v \frac{dT_{op}}{dt} = \int_0^{L_{op}} h_{q,B} T_B ds - T_{op} \int_0^{L_{op}} h_{q,B} ds. \tag{12}$$

Equation (12) represent the basis to determine air temperature inside the opening and is solved iteratively, based on the temperature of the boundary surface from the previous time step.

For the exchange of moisture between the two subsystems Eq. (6) is applied.

2.2 Basic Equations of Mechanical Model

In this section the second phase of the fire analysis of the HC slab is presented, where the mechanical response of the HC slab simultaneously exposed to external mechanical and fire load is determined. Mathematical model to describe the deformation of concrete part of the HC slab is based on the Reissner exact beam theory (Reissner 1972), while the behaviour of prestressing tendon is simplified with the wire model. To interconnect these two systems (concrete part and tendon) constraining equations are introduced, allowing for the tangential slip at the contact between concrete and tendon, while neglecting the normal separation. Further on, mechanical properties of the contact between concrete and tendon are temperature dependent. Mechanical and rheological properties of concrete and prestressing steel are temperature dependent as well. Another important feature of the model is considering additive decomposition of the increment of the extensional strain of random concrete fiber, being composed of the increment of mechanical, temperature, creep and transient strain: $\Delta\varepsilon_c = \Delta\varepsilon_{\sigma,c} + \Delta\varepsilon_{th,c} + \Delta\varepsilon_{cr,c} + \varepsilon_{tr,c}$. Similarly, increment of extensional strain of tendon consists of the increment of mechanical, temperature and thermal-creep strain which occur due to the viscous creep of steel at elevated temperatures: $\Delta\varepsilon_p = \Delta\varepsilon_{\sigma,p} + \Delta\varepsilon_{th,p} + \Delta\varepsilon_{cr,p}$. Although the mechanical model is based on a physically highly precise description of the problem, there are two

assumptions that somewhat simplify model a bit. First one is neglecting tension strength of concrete since it does not have a significant influence on load-bearing capacity of the HC slab. Second one is disregarding the influence of shear strain on the deformation of the HC slab given the fact that the span of the HC slab is usually by factor of 25 or more greater than the height of the HC slab, meaning that shear strain does not have considerable influence.

To better understand model derivation and basic quantities involved, undeformed and deformed configuration of prestressed beam is given in Fig. 2. Concrete beam with the initial length L and constant cross-section A_c is prestressed by n_p tendons, that are symmetrically distributed over the cross-section. Cross section of each tendon is labelled as $A_p^k\,(k = 1, 2, \ldots, n_p)$, ϕ_p^k is the tendon diameter, while $N_{p,0}^k$ denotes the initial prestressing force of individual tendon. The reference axis of the concrete part of beam is in the centre of the cross-section of the beam, while the reference axis of the kth tendon is in the centre of the cross-section of each tendon.

When setting the governing equations of the mathematical model the derivation can be simplified by introducing a material coordinate x_p^{*k} which determines a particle of the kth tendon in undeformed configuration (point Q_p^k) that is in contact with a particle of concrete in deformed configuration whose material coordinate is x_c (point T_c^k) (see Fig. 2). This means that the particles of concrete (point T_c^k) and kth tendon (point T_p^k), which in undeformed state coincide, occupy different points in space in deformed configuration, i.e. slip $\Delta^k(x_c)$ between them occurs. Since the tendon dimension are relatively small it is simplified that $z_p^k = z_c^k$. Considering the fact that the slips between concrete and tendon are relatively small, it is further assumed:

$$(\bullet)_p^{*k} \approx (\bullet)_p^k \quad \text{and} \quad \int_{0^*}^{L^*} (\bullet)_p^{*k}\,\mathrm{d}x^* \approx \int_0^L (\bullet)_p^k\,\mathrm{d}x,\ (k = 1, 2, \ldots, n_p). \tag{13}$$

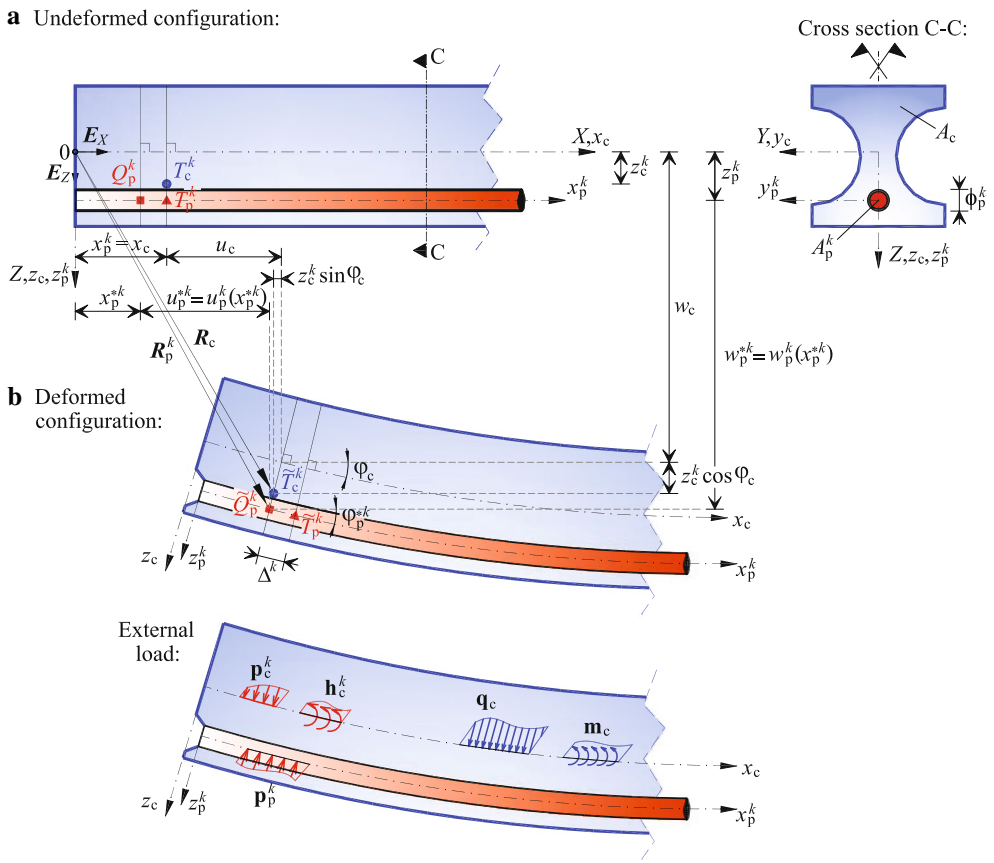

Fig. 2 Undeformed (reference) and deformed (current) configuration of prestressed concrete beam.

which means that differences between functions determined at x^* and x are insignificant for any $k = 1, 2, \ldots, n_p$.

2.2.1 The Stress–Strain Field

The basic equations of prestressed concrete beam subjected to fire are composed of kinematic, constraining and equilibrium equations. In addition, constitutive equations and corresponding constitutive laws are needed to consider properties of each material.

In accordance to the Reissner planar beam model, the kinematic equations written separately for concrete part of the beam and tendon are as follows (see Markovič et al. 2013):

$$\text{concrete part of the beam: } 1 + u_{\mathrm{c}}' - (1 + \varepsilon_{\mathrm{c0}}) \cos \varphi_{\mathrm{c}} = 0, \tag{14}$$

$$w_{\mathrm{c}}' + (1 + \varepsilon_{\mathrm{c0}}) \sin \varphi_{\mathrm{c}} = 0, \tag{15}$$

$$\varphi_{\mathrm{c}}' - \kappa_{\mathrm{c}} = 0, \tag{16}$$

$$\text{tendon: } 1 + {u_{\mathrm{p}}}^{k\prime} - \left(1 + \varepsilon_{\mathrm{p}}^{k}\right) \cos \varphi_{\mathrm{p}}^{k} = 0, \quad (k = 1, 2, \ldots, n_{\mathrm{p}}). \tag{17}$$

Here $(\bullet)'$ represents a derivative of selected quantity with the respect to material coordinate x_{c} (see Fig. 2), quantities u_{c} and w_{c} denote horizontal and vertical displacement of a random point on the reference axis of concrete part of the beam, similarly, u_{p}^{k} is horizontal displacement of the reference axis of kth tendon. $\varepsilon_{\mathrm{c0}}$ and κ_{c} are extensional strain and pseudo-curvature of the reference axis of the concrete part of the beam, while φ_{c} represent the rotation of the concrete cross-section. The geometrical strain of concrete part of the section is thus determined as: $\varepsilon_{\mathrm{c}} = \varepsilon_{\mathrm{c0}} + z_c \kappa_{\mathrm{c}}$. The extensional strain of k^{th} tendon and the rotation of the k^{th} tendon cross-section are denoted as $\varepsilon_{\mathrm{p}}^{k}$ and φ_{p}^{k}, respectively.

The constraining equations provide the description of the interaction at the contact between concrete and k^{th} tendon. Considering the simplification that $z_{\mathrm{p}}^{k} = z_{\mathrm{c}}^{k}$, than vectors describing the deformed position of the chosen particle of concrete beam (point T_{c}^{k}) and tendon (point Q_{p}^{k}) at the contact become the same.

$$\boldsymbol{R}_{\mathrm{c}} = \boldsymbol{R}_{\mathrm{p}}^{k} \tag{18}$$

In component form, Eq.(18) can be written:

$$x_{\mathrm{c}} + u_{\mathrm{c}} + z_{\mathrm{c}}^{k} \sin \varphi_{\mathrm{c}} = x_{\mathrm{p}}^{*k} + u_{\mathrm{p}}^{*k} \approx x_{\mathrm{p}}^{*k} + u_{\mathrm{p}}^{k}, \tag{19}$$

$$w_{\mathrm{c}} + z_{\mathrm{c}}^{k} \cos \varphi_{\mathrm{c}} = w_{\mathrm{p}}^{*k} \approx w_{\mathrm{p}}^{k}. \tag{20}$$

where w_{p}^{k} represents vertical displacement of the reference axis of kth tendon. Slip at the contact between concrete and kth tendon (see Fig. 2) is given by the following equation:

$$\Delta^{k}(x_{\mathrm{c}}) = \int_{x_{\mathrm{p}}^{*k}}^{x_{\mathrm{c}}} (1 + \varepsilon_{\mathrm{p}}^{k}) \mathrm{d}x, \quad (k = 1, 2, \ldots, n_{\mathrm{p}}). \tag{21}$$

Based on the constraining equations (Eqs. 19 and 20) and kinematic equations (Eqs. 14–17) and taking into account the assumptions (13), the following relationships can be given:

$$\varphi_{\mathrm{p}}^{k} = \varphi_{\mathrm{c}} \quad \text{and} \quad \kappa_{\mathrm{p}}^{k} = \frac{1 + \varepsilon_{\mathrm{p}}^{k}}{1 + \varepsilon_{\mathrm{c0}} + z_{\mathrm{c}}^{k} \kappa_{\mathrm{c}}} \kappa_{\mathrm{c}}. \tag{22}$$

The above equations simplifies the rotation of tendon cross-section, making it equal to the rotation of concrete part of the cross-section while the pseudo-curvature of the reference axis of the kth tendon κ_{p}^{k} can be determined via trivial expression.

The equilibrium equations deliver the relationship between beam internal forces and external load. Internal forces in the concrete part of the beam are represented by equilibrium axial and shear force ($\mathscr{N}_{\mathrm{c}}$, $\mathscr{Q}_{\mathrm{c}}$) and by equilibrium bending moment $\mathscr{M}_{\mathrm{c}}$, $\mathscr{N}_{\mathrm{p}}^{k}$ is the equilibrium axial force of the kth tendon. It is assumed that the external load acts along the beam reference axis and is presented by conservative line traction $\boldsymbol{q}_{\mathrm{c}} = q_{X,\mathrm{c}} \boldsymbol{E}_X + q_{Z,\mathrm{c}} \boldsymbol{E}_Z$ and moment traction $\boldsymbol{m}_{\mathrm{c}} = m_{Y,\mathrm{c}} \boldsymbol{E}_Y$ (see Fig. 2). At the contact between concrete and tendon contact load is considered. Loads $\boldsymbol{p}_{\mathrm{c}}^{k} = p_{X,\mathrm{c}}^{k} \boldsymbol{E}_X + p_{Z,\mathrm{c}^k} \boldsymbol{E}_Z$ and $\boldsymbol{h}_{\mathrm{c}}^{k} = p_{X,\mathrm{c}}^{k} z_{\mathrm{c}}^{k} \boldsymbol{E}_Y$ represent the impact of tendon on the concrete part of the beam. On the other hand, the influence of concrete on tendon is, due to the wire model, expressed only by line load $\boldsymbol{p}_{\mathrm{p}}^{k} = p_{X,\mathrm{p}}^{k} \boldsymbol{E}_X + p_{Z,\mathrm{p}}^{k} \boldsymbol{E}_Z$, where the equilibrium of contact forces must be met, namely:

$$p_{X,\mathrm{p}}^{k} + p_{X,\mathrm{c}}^{k} = 0 \tag{23}$$

$$p_{Z,\mathrm{p}}^{k} + p_{Z,\mathrm{c}}^{k} = 0, \quad (k = 1, 2, \ldots, n_{\mathrm{p}}). \tag{24}$$

The equilibrium equations are:

$$\text{concrete part of the beam: } \mathscr{R}_{X,c'} + q_{X,\mathrm{c}} + \sum_{k=1}^{n_{\mathrm{p}}} p_{X,\mathrm{c}}^{k} = 0, \tag{25}$$

$$\mathscr{R}_{Z,c'} + q_{Z,\mathrm{c}} + \sum_{k=1}^{n_{\mathrm{p}}} p_{Z,\mathrm{c}}^{k} = 0, \tag{26}$$

$$\mathscr{M}_{\mathrm{c}}' - (1+\varepsilon_{\mathrm{c0}})\mathscr{Q}_{\mathrm{c}} + m_{Y,\mathrm{c}} + \sum_{k=1}^{n_{\mathrm{p}}} p_{X,\mathrm{c}}^{k} z_{\mathrm{c}}^{k} = 0, \tag{27}$$

$$\text{tendon: } \mathscr{N}_{\mathrm{p}}{}^{k\prime} + p_{\mathrm{t,p}}^{k} = 0, \qquad (k = 1, 2, \ldots, n_{\mathrm{p}}), \tag{28}$$

$$p_{\mathrm{n,p}}^{k} - \mathscr{N}_{\mathrm{p}}^{k}\kappa_{\mathrm{p}}^{k} = 0, \quad (k = 1, 2, \ldots, n_{\mathrm{p}}). \tag{29}$$

In Eqs. (25) and (26) $\mathscr{R}_{X,\mathrm{c}}$ and $\mathscr{R}_{Z,\mathrm{c}}$ denotes the equilibrium horizontal and vertical component of the internal forces $\mathscr{N}_c$ and $\mathscr{Q}_c$. They are related as: $\mathscr{R}_{X,\mathrm{c}} = \mathscr{N}_c \cos\varphi_{\mathrm{c}} + \mathscr{Q}_c \sin\varphi_{\mathrm{c}}$ and $\mathscr{R}_{Z,\mathrm{c}} = -\mathscr{N}_c \sin\varphi_{\mathrm{c}} + \mathscr{Q}_c \cos\varphi_{\mathrm{c}}$. $p_{\mathrm{n,p}}^{k}$ in $p_{\mathrm{t,p}}^{k}$ are so-called normal and tangential components of the contact load for the kth tendon defined in the material basis $(x_{\mathrm{p}}^{k}, z_{\mathrm{p}}^{k})$. They are linked to the components of contact load in a fixed Cartesian coordinate system as: $p_{\mathrm{n,p}}^{k} = p_{X,\mathrm{p}}^{k}\sin\varphi_{\mathrm{c}} + p_{Z,\mathrm{p}}^{k}\cos\varphi_{\mathrm{c}}$ and $p_{\mathrm{t,p}}^{k} = p_{X,\mathrm{p}}^{k}\cos\varphi_{\mathrm{c}} - p_{Z,\mathrm{p}}^{k}\sin\varphi_{\mathrm{c}}$.

2.2.2 Constitutive Equations and Constitutive Laws

Constitutive equations interconnect equilibrium quantities with the deformation quantities:

$$\text{concrete part of the beam: } \mathscr{N}_{\mathrm{c}} = \mathscr{N}_{\mathrm{c,c}} = \int_{A_{\mathrm{c}}} \sigma_{\mathrm{c}}\mathrm{d}A_{\mathrm{c}}, \tag{30}$$

$$\mathscr{M}_{\mathrm{c}} = \mathscr{M}_{\mathrm{c,c}} = \int_{A_{\mathrm{c}}} z_{\mathrm{c}}\sigma_{\mathrm{c}}\mathrm{d}A_{\mathrm{c}}, \tag{31}$$

$$\text{tendon: } \mathscr{N}_{\mathrm{p}}^{k} = \mathscr{N}_{\mathrm{c,p}}^{k} = \sigma_{\mathrm{p}}^{k}A_{\mathrm{p}}^{k} \quad (k = 1, 2\ldots, n_{\mathrm{p}}). \tag{32}$$

Above, $\sigma_{\mathrm{c}}(\varepsilon_{\sigma,\mathrm{c}}, T)$ and $\sigma_{\mathrm{p}}^{k}(\varepsilon_{\sigma,\mathrm{p}}^{k}, T)$ denote normal physical stresses in concrete and k^{th} tendon, which are function only of the mechanical strain and temperature. The stress–strain relationship is given by the chosen constitute law. In addition, the constitutive law of slip must be defined in order to determine the relationship between slip Δ^k and shear stress $p_{\mathrm{t,c}}^{k}$ at the contact between concrete and kth tendon. In what follows the chosen constitute laws for concrete, prestressing steel and contact are presented.

The behaviour of concrete in compression at elevated temperatures is described by the constitutive law found in EN 1992-1-2 (see Fig. 3a). Load bearing capacity of concrete in tension is neglected. Temperature dependent material parameters are compressive strength $f_{\mathrm{c,T}}$, the corresponding strain $\varepsilon_{\mathrm{c1,T}}$ and the ultimate compressive strain $\varepsilon_{\mathrm{cu1,T}}$. Further on, the constitutive law given in EN 1992-1-2 (see Fig. 3b) is used to represent the behaviour of tendon in tension and compression. Here the temperature dependent material parameters of prestressing steel are the maximum stress level $f_{\mathrm{py,T}}$, the corresponding strain $\varepsilon_{\mathrm{pt,T}}$, the proportional limit $f_{\mathrm{pp,T}}$, the modulus of elasticity $E_{\mathrm{p,T}}$ and the ultimate strain $\varepsilon_{\mathrm{pu,T}}$. In constitutive models for both materials, the isotropic hardening is accounted for. The unloading slope is linear and equal to the current modulus of elasticity. For concrete this is a secant modulus of elasticity $E_{\mathrm{cm,T}} = 0.4 f_{\mathrm{c,T}}/(0.2693\,\varepsilon_{\mathrm{c1,T}})$, while for prestressing steel this is $E_{\mathrm{p,T}}$.

The idealized multilinear law introduced by Keuser and Mehlhorn (1983) describes the relationship between the shear stress $p_{\mathrm{t,c}}^{k}$ and slip Δ^k at the contact between concrete and kth tendon (see Fig. 3c). It is applied that $p_{\mathrm{t,c}}^{k} = \pi\,\phi_{\mathrm{p}}^{k}\,\tau^{k}$ $(k = 1, 2, \ldots, n_{\mathrm{p}})$, where τ^k represents the bond stress at concrete-tendon contact. Temperature dependent material parameters are bond stresses $\tau_{1,T}$, $\tau_{2,T}$ and the bond strength $\tau_{\mathrm{u,T}}$ (see Khalaf and Huang 2016).

In the cooling phase it is assumed that the concrete does not recover the compressive strength, the same is applied for the bond strength, while prestressing steel fully recovers its strength. Additional assumption is made by considering temperature strains of steel as fully reversal. Creep of concrete is the same in heating and cooling phase, while the viscous creep of steel in cooling phase is disregarded. Likewise, the transient strain of concrete is not accounted for in the cooling phase (Bratina et al. 2007).

2.2.3 Boundary Conditions

A set of kinematic, equilibrium and constitutive equations is supplemented by the corresponding static and kinematic boundary conditions:

$$\text{concrete part: } S_{1,\mathrm{c}} + \mathscr{R}_{\mathrm{X,c}}(0) = 0 \quad \text{or} \quad u_{1,\mathrm{c}} = u_{\mathrm{c}}(0), \tag{33}$$

$$S_{2,\mathrm{c}} + \mathscr{R}_{\mathrm{Z,c}}(0) = 0 \quad \text{or} \quad u_{2,\mathrm{c}} = w_{\mathrm{c}}(0), \tag{34}$$

$$S_{3,\mathrm{c}} + \mathscr{M}_{\mathrm{c}}(0) = 0 \quad \text{or} \quad u_{3,\mathrm{c}} = \varphi_{\mathrm{c}}(0), \tag{35}$$

$$S_{4,\mathrm{c}} - \mathscr{R}_{\mathrm{X,c}}(L) = 0 \quad \text{or} \quad u_{4,\mathrm{c}} = u_{\mathrm{c}}(L), \tag{36}$$

$$S_{5,\mathrm{c}} - \mathscr{R}_{\mathrm{Z,c}}(L) = 0 \quad \text{or} \quad u_{5,\mathrm{c}} = w_{\mathrm{c}}(L), \tag{37}$$

$$S_{6,\mathrm{c}} - \mathscr{M}_{\mathrm{c}}(L) = 0 \quad \text{or} \quad u_{6,\mathrm{c}} = \varphi_{\mathrm{c}}(L), \tag{38}$$

$$\text{tendon: } \mathscr{N}_{\mathrm{p}}^{k}(0) = 0 \quad \text{or} \quad u_{1,\mathrm{p}}^{k} = u_{\mathrm{p}}^{k}(0), \quad (k = 1, 2\ldots, n_{\mathrm{p}}), \tag{39}$$

$$\mathscr{N}_{\mathrm{p}}^{k}(L) = 0 \text{ or } u_{4,\mathrm{p}}^{k} = u_{\mathrm{p}}^{k}(L), \quad (k = 1, 2\ldots, n_{\mathrm{p}}). \tag{40}$$

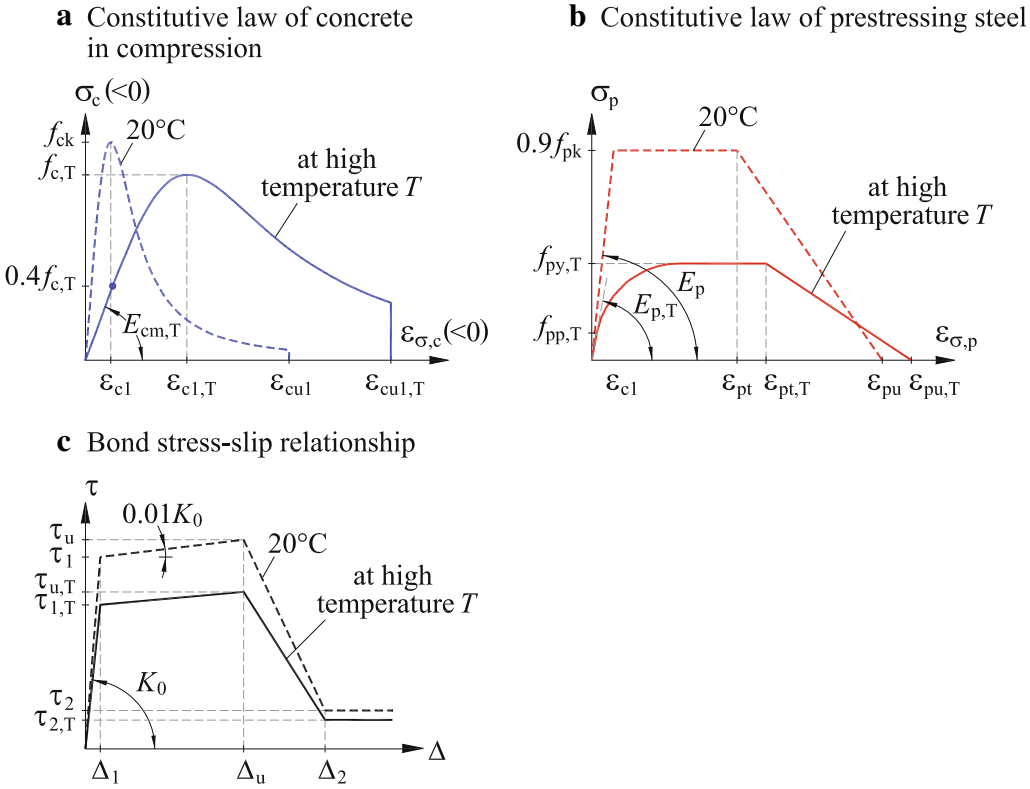

Fig. 3 Constitutive law of **a** concrete in compression, **b** prestressing steel and **c** bond slip.

In Eqs. (33–38), $u_{i,\mathrm{c}}$ $(i = 1, \ldots, 6)$ and $u^k_{j,\mathrm{p}}$ $(j = 1 \text{ or } 4)$ denote the given values of the boundary displacements, similarly $S_{i,\mathrm{c}}$ $(i = 1, \ldots, 6)$ mark given forces at the beginning and at the end of the concrete part of the beam.

3 Numerical Solution

3.1 Coupled Hygro-Thermo-Chemical Model

The solution of three partial differential equations describing the transfer of dry air, moisture and energy conservation, together with boundary and initial conditions is obtained numerically using finite element method based on Galerkin discretisation. Difference scheme is used for time discretisation, where the entire computational time domain is divided on time increments $\left[t^{i-1}\ t^i\right]$. Implicit time difference scheme is used to solve governing equations within each time step. A more detailed description of the finite element formulation is given in (Davie et al. 2006; Hozjan 2009).

3.2 Mechanical model

Mathematical model presented in Sect. 2.2 is solved numerically with the finite element method. Strain-based finite element is employed (Bratina et al. 2004; Markovič et al. 2013), where the unknown strain functions $(\varepsilon_{\mathrm{c}0}, \kappa_{\mathrm{c}}, \varepsilon^k_{\mathrm{p}})$, unknown coordinates x^{*k}_{p} and the normal component of the unknown contact load $p^k_{\mathrm{n,p}}$ are interpolated over the finite element by Lagrangian interpolation polynomials with N interpolation points. The total time of fire analysis $\left[0,\ t^{\mathrm{end}}\right]$ is divided into time increments $\left[t^{i-1},\ t^i\right]$. The system of algebraic equations of the prestressed concrete beam finite element at time t^i consists of $N(2 + 3n_{\mathrm{p}}) + (9 + 3n_{\mathrm{p}})$ equations for the same number of unknowns: $N(2 + n_{\mathrm{p}})$ unknown deformation nodal values $(\varepsilon^i_{\mathrm{c}0,n},\ \kappa^i_{\mathrm{c},n},\ \varepsilon^{k,i}_{\mathrm{p},n})$, $N(2n_{\mathrm{p}})$ unknown nodal values of variables $x^{*k,i}_{\mathrm{p},n}$ and $p^{k,i}_{\mathrm{n,p},n}$ $(n = 1, 2, \ldots, N)$, $(3 + n_{\mathrm{p}})$ unknown equilibrium values $(\mathscr{R}^i_{\mathrm{X,c}}(0),\ \mathscr{R}^i_{\mathrm{Z,c}}(0),\ \mathscr{M}^i_{\mathrm{c}}(0),\ \mathscr{N}^{k,i}_{\mathrm{p}}(0))$ and $(6 + 2n_{\mathrm{p}})$ unknown nodal displacements and the rotations $(u^i_{\mathrm{c}}(0),\ w^i_{\mathrm{c}}(0),\ \varphi^i_{\mathrm{c}}(0),\ u^{k,i}_{\mathrm{p}}(0),\ u^i_{\mathrm{c}}(L),\ w^i_{\mathrm{c}}(L),\ \varphi^i_{\mathrm{c}}(L)$ and $u^{k,i}_{\mathrm{p}}(L))$. Hereafter the $N(2 + 3n_{\mathrm{p}})$ internal degrees of freedom of finite elements $(\varepsilon^i_{\mathrm{c}0,n},\ \kappa^i_{\mathrm{c},n},\ \varepsilon^{k,i}_{\mathrm{p},n},\ x^{*k,i}_{\mathrm{p},n}$ and $p^{k,i}_{\mathrm{n,p},n})$ are condensed, while the remaining degrees of freedom are combined into the structure equation:

$$\boldsymbol{G}\left(x^i,\ \lambda^i,\ T^i,\ t^i\right) = 0\,. \tag{41}$$

where vector x^i represents the equilibrium quantities and nodal displacements and rotations of the finite element

at the time t^i, parameter λ^i is load factor for structure at time t^i and T^i is temperature field at the same time. Equation (41) is solved by Newton increment-iterative method.

In the subsequent the detailed procedure to compute the mechanical strain of concrete $\varepsilon_{\sigma,c}$ and kth tendon $\varepsilon^k_{\sigma,p}$ at the end of time increment $\left[t^{i-1},\ t^i\right]$ is presented. It is assumed that within time interval $\left[t^{i-1},\ t^i\right]$ the stress–strain state is firstly determined at time t^{i-1}. In order to compute stress–strain state at time t^i, new temperature field in concrete T^i at time t^i has to be calculated, based on the hygro-thermo-chemical analysis. Employing this results into the mechanical model, the extensional strain of individual concrete fibre or kth tendon at t^i can be given as:

$$\varepsilon^i_c = \varepsilon^{i-1}_c + \Delta\varepsilon^i_c, \tag{42}$$

$$\varepsilon^{k,i}_p = \varepsilon^{k,i-1}_p + \Delta\varepsilon^{k,i}_p, \tag{43}$$

where $\Delta\varepsilon^i_{c(p)}$ represent the increment of extensional strain within time interval $[t^{i-1},\ t^i]$. Using the aforementioned additive decomposition, the increment of mechanical strain in concrete fibre or kth tendon yields to:

$$\begin{aligned}\Delta\varepsilon^i_{\sigma,c} = {} & \Delta\varepsilon^i_c - \Delta\varepsilon^i_{th,c}(T^i) - \Delta\varepsilon^i_{cr,c}(\sigma^i_c, T^i, t^i) \\ & - \Delta\varepsilon^i_{tr,c}(\sigma^i_c, \varepsilon^i_{th,c}, T^i),\end{aligned} \tag{44}$$

$$\Delta\varepsilon^{k,i}_{\sigma,p} = (\varepsilon^k_{p,0}) + \Delta\varepsilon^{k,i}_p - \Delta\varepsilon^{k,i}_{th,p}(T^i) - \Delta\varepsilon^{k,i}_{cr,p}(\sigma^{k,i}_p, T^i, t^i), \quad (k = 1, 2 \ldots, n_p), \tag{45}$$

meaning that the mechanical strain at time t^i is:

$$\varepsilon^i_{\sigma,c} = \varepsilon^{i-1}_{\sigma,c} + \Delta\varepsilon^i_{\sigma,c}, \tag{46}$$

$$\varepsilon^{k,i}_{\sigma,p} = \varepsilon^{k,i-1}_{\sigma,p} + \Delta\varepsilon^{k,i}_{\sigma,p}, \quad (k = 1, 2 \ldots, n_p). \tag{47}$$

where $\varepsilon^k_{p,0}$ denotes the initial deformation of k^{th} tendon at time t^0 due to the initial prestressing force ($\varepsilon^k_{p,0} = N^k_{p,0}/E_p A^k_p$). Detailed description of each strain increment is given in Bratina et al. (2007). It should be noted, that some strain increments are also a function of stress at given time, meaning that iterative computation is needed on order to determine some of the stress and strain increments within time interval $[t^{i-1},\ t^i]$.

4 Numerical Example

4.1 Validation of Presented Model for Natural Fire

The main emphasis of this part of numerical example is the validation of the presented numerical model with the experimental results provided by Bailey and Lennon (2008). In their research, two large-scale natural fire tests (Test 1 and Test 2) on the HC slabs were performed. Figure 4 shows geometric and material data and mechanical load acting on the analysed HC slabs. Each HC slab was prestressed by seven tendons with the nominal diameter $\phi_p = 12.5$ mm ($A_p = 93\,mm^2$). Tensile strength of tendon was not reported in Bailey and Lennon (2008), therefore, the assumed value was $f_{p0.1k}/f_{pk} = 1670/1860$ MPa which represents the strength of the most widely used prestressing steel. In addition, there was no data about the level of initial prestressing force. It was considered in the analysis, that the stress in each tendon at the beam midspan, prior fire occurrence, was equal to $\sigma^1_p = 0.52 f_{p0.1k}$. Characteristic compressive strength of concrete given in Bailey and Lennon (2008) is 86 MPa (tested on cube). The HC slab is modelled as simply supported beam with the span of 7.0 m and loaded with line traction $q_{Z,c} = 9.2$ kN/m (self-weight plus applied load).

Different quantities were measured during the experiment, the chosen ones for the validation are development of temperatures within the HC slab and the development of midspan vertical displacement. Since natural fire is designed, it is important to note that the validation is done also for the cooling phase. As already described before, the response of the HC slab exposed to fire with presented numerical model, is divided in two general steps.

4.1.1 Hygro-Thermo-Chemical Analysis of the HC Slab

The HC slab was subjected to natural fire (Test 1 and Test 2) from the bottom side. Measured development of temperatures within the fire compartment for both tests is given in Fig. 5a. Maximum gas temperature is similar in both tests (1069 °C at 52 min in Test 1 and 1047 °C at 62 min in Test 2). However, temperature increase is slightly faster in Test 1. Figure 5b demonstrates the development of temperature in tendon at the HC slab midspan for Test 1.

It is presumed, that temperature along the HC slab is uniform, therefore hygro-thermo-chemical analysis is performed only over the HC slab cross-section. Further on, due to the symmetry of the cross-section with the respect to Z axis, only one-sixth of the cross-section is analysed (see Fig. 6), assuming zero moisture and heat flow along the cut edges (Edge 2 on Fig. 6).

The part of the cross-section is modelled with 114 four-node isoparametric quadrilateral finite elements. The effect of tendon on hygro-thermo-chemical analysis is neglected (CEN 2005). Thermal conductivity for the hygro-thermo-chemical analysis is described with equation $k = 1.7 - 0.19 \times T/100 + 0.008 \times (T/100)^2$ and takes place between upper and lower limit of thermal conductivity as given in CEN (2005). The values of surface emissivity and convection coefficient are taken according (CEN 2004). On the exposed side (Edge 1) surface emissivity of concrete and convection coefficient are $\varepsilon = 0.7$ and $h_q = 25$ W/m^{2}K, respectively. On the unexposed side

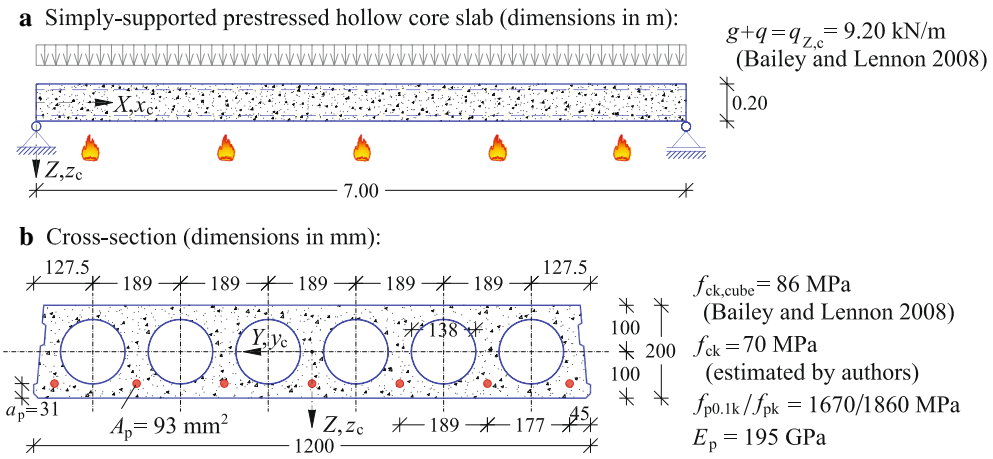

Fig. 4 HC slab: geometry and material data.

(Edge 3) convection coefficient is $h_q = 9$ W/m^{2}K, the same applies to the opening, i.e. Edge 4, where $h_{q,B} = 9$ W/m^{2}K. Boundary conditions are summarized in Table 1. The remaining data for the hygro-thermo-chemical analysis are: density of cement $\rho_{\text{cem}} = 300$ kg/m^3, density of concrete $\rho_{\text{c}} = 2400$ kg/m^3, initial temperature $T_0 = 20$ °C, initial pore pressure $P_{G,0} = 0.1$ MPa, initial water vapour content $\tilde{\rho}_{V,0} = 0.07$ kg/m^3, water vapour content on boundary $\tilde{\rho}_{V,\infty} = 333$ kg/m^3, initial permeability of concrete $K = 1{\times}10^{-16}$, initial porosity of concrete $p_{\text{or},0} = 0.1$ and initial free water amount $\bar{\rho}_{FW,0} = 70$ kg/m^3.

Three simulations are performed with advanced hygro-thermo-chemical model (Hozjan et al. 2010). Input data as well as boundary conditions for the first case S1 is presented above. Second case S2 assumes different boundary condition in the opening ($q_T = q_T(T_0)$), meaning that the temperature inside the opening remains T_0 during simulation. In the third case S3 the heat and mass flux into the opening is prevented, meaning that the opening is isolated from the rest of the cross-section. The corresponding boundary conditions on Edge 4 for this case are: $\frac{\partial T}{\partial n} = 0$, $\frac{\partial P_G}{\partial n} = 0$, $\frac{\partial \bar{\rho}_V}{\partial n} = 0$.

Figure 7a, b demonstrate development of calculated temperatures in concrete at tendon position for all three analysed cases (S1, S2, S3), separately for Test 1 and Test 2. Hatched area represents the temperature distribution in concrete at tendon position for case S1. The upper boundary of hatched area is the temperature in concrete at the bottom of tendon ($a_{\text{p}} - \phi_{\text{p}}/2$), while the bottom boundary of the hatched area is concrete temperature determined at the top of tendon ($a_{\text{p}} + \phi_{\text{p}}/2$). Supplementary, Fig. 7a shows development of measured temperatures at tendon position. The measured temperature at tendon position from Test 2 is not given in Fig. 7b, since it was not measured in the experiment.

By comparing calculated temperatures (cases S1, S2, S3) with each other, the following can be observed: (i) development of temperatures with time in the heating phase (52 min in Test 1 and 62 min in Test 2) for all three considered cases (S1–S3) is almost equal. This implies,

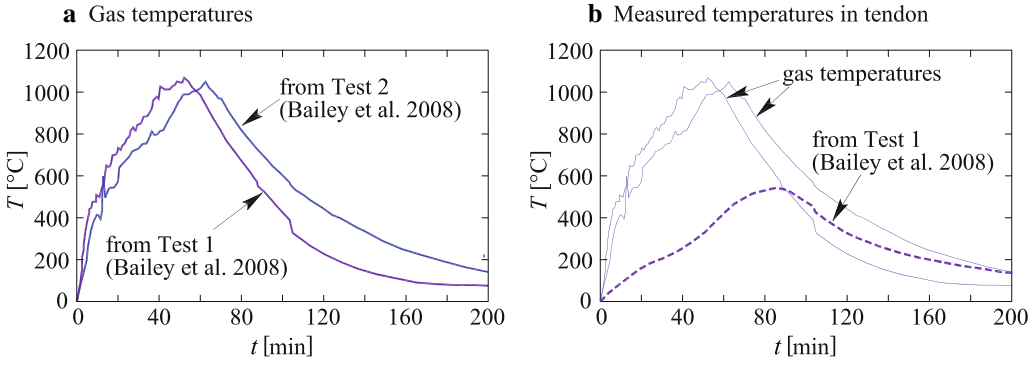

Fig. 5 **a** Development of gas temperatures in fire compartment for Test 1 and 2, **b** development of temperatures at the tendon location with time for Test 1.

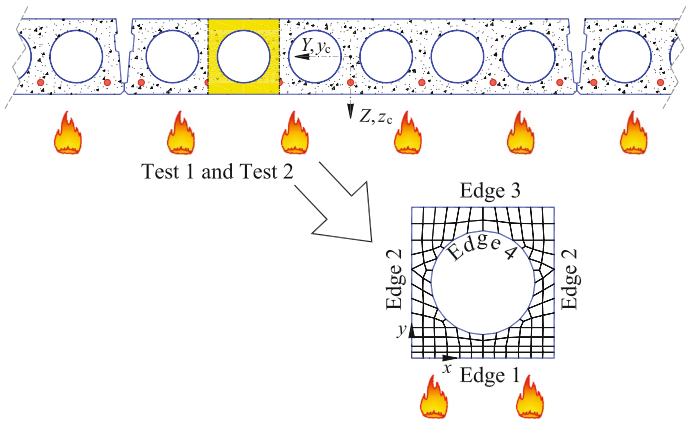

Fig. 6 The HC slab cross-section geometry and finite element mesh to determine the distribution of temperatures.

that considering the opening in the hygro-thermo-chemical analysis does not have a significant impact on distribution of temperatures in the heating phase, (ii) in the cooling phase opening acts as an energy sink and has a considerable impact on temperature development. Thus, the most rapid temperature decrease is observed in case S2, when the temperature in the opening is equal to the initial one throughout the entire simulation. On the other hand, the slowest decrease occurs in case S3, when the opening is isolated, i.e. when heat and mass flux in the opening is prevented, (iii) in average the calculated temperatures in the heating phase are lower in Test 2 than in Test 1 (see Fig. 7b), while the opposite is identified in the cooling phase. This arise due to the slower temperature increase within fire compartment in Test 2, while the gas temperatures in the cooling phase were a bit higher compare to the Test 1 (see Fig. 5).

Next conclusions can be given by comparing numerically and experimentally determined temperatures: (i) minor discrepancies are observed when comparing temperature developments in heating phase. The reason for this might be different measuring position as it was reported in Bailey and Lennon (2008), (ii) experimentally measured temperature decrease in cooling phase is faster than in cases S1, S2 and S3. As described in Bailey and Lennon (2008), cracks occurred at the measuring point (midspan of the HC slab). Therefore, heat flux throughout cracked zone increased, which led to the faster decrease of temperatures. However, cracking of concrete in numerical formulation is not taken into consideration. Thus, calculated temperature decrease is slower compared to the measurements.

4.1.2 Mechanical Analysis

The HC slab is modelled as simply supported beam with the span of 7.0 m and loaded with line traction $q_{Z,c} = 9.2\,\text{kN/m}$, as shown in Fig. 4. Beam is discretized with 36 finite elements (see Fig. 8a). To ensure the computation stability, short constant-strain elements are used (Bratina et al. 2004), meaning that the strain quantities in the concrete part of the beam are constant along each element ($\varepsilon_{c0} = \text{const.}, \kappa_c = \text{const.}$). Due to the symmetry, only one-sixth of the cross-section is considered and divided on 31 rectangular fields, inside each, 3×3 Gauss integration scheme is applied to determine the distribution of normal stresses over the concrete cross-section (see Fig. 8b, c). Prestressing tendon is considered as a point.

As stated before, the behaviour of concrete and tendon at elevated temperatures is described by the constitutive laws proposed by CEN (2005), presented on Fig. 3a and b. The HC slabs were composed of high strength concrete, therefore, temperature dependency of compression strength $f_{c,T}$ in the analysis is taken for high strength concrete class 2 (see Fig. 9). However, material parameters $\varepsilon_{c1,T}$ and $\varepsilon_{cu1,T}$ are considered according to the normal weight concrete. The properties of cold worked class B prestressing steel are used to describe the material parameters of tendon at elevated temperatures. Reduction of strength with temperature for maximum stress level $f_{py,T}$ is shown in Fig. 9. In the applied constitutive law for prestressing steel, creep strain of steel $\varepsilon_{cr,p}$ is combined with the plastic strain. Together they form inelastic strain. For this reason, explicit formulation of creep strain increment is not necessary. Therefore, $\Delta\varepsilon_{cr,p} = 0$. For concrete, creep strain increment $\Delta\varepsilon_{cr,c}$ is explicitly expressed by the formulation given by Harmathy (1967). Further on, transient strain increment for concrete $\Delta\varepsilon_{tr,c}$ is proposed by Anderberg and Thelandersson (1976). Thermal strain increments for concrete $\Delta\varepsilon_{th,c}$ and prestressing steel $\Delta\varepsilon_{th,p}$ are taken in accordance with CEN (2005). Finally, the material parameters

Table 1 Boundary conditions for Edges 1, 2, 3 and 4.

	Edge 1	Edge 2	Edge 3	Edge 4
T:	$q_T = q_T$(Test 1, Test 2)	$\frac{\partial T}{\partial n} = 0$	$q_T = q_T(T_\infty = 20°C)$	$q_T = q_T(T_{op})^a$
P_G:	$P_G = 0.1$MPa	$\frac{\partial P_G}{\partial n} = 0$	$P_G = 0.1$	$P_G = 0.1^a$
$\tilde{\rho}_V$:	$q_v = q_v(\tilde{\rho}_{V,\infty})$	$\frac{\partial \tilde{\rho}_V}{\partial n} = 0$	$q_v = q_v(\tilde{\rho}_{V,\infty})$	$q_v = q_v(\tilde{\rho}_{V,\infty})^a$

[a] Boundary conditions for case S1.

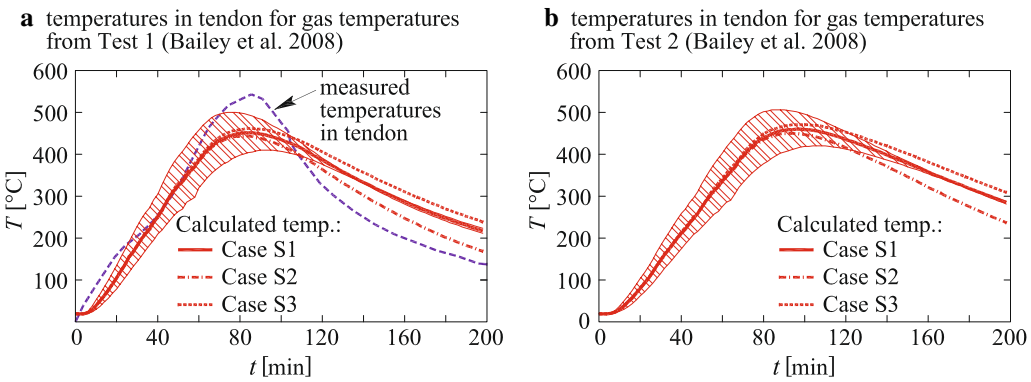

Fig. 7 Development of temperatures in concrete at tendon position with time: **a** in Test 1, **b** in Test 2.

for the constitutive law of contact (see Fig. 3c), are as follows (Keuser and Mehlhorn 1983): $\tau_1 = 5$ MPa, $\tau_u = 5.45$ MPa and $\tau_2 = 0.5$ MPa. Temperature dependency of these parameters is adopted from Diederichs and Schneider (1981) and shown for $\tau_{u,T}$, $\tau_{1,T}$ and $\tau_{2,T}$ in Fig. 9.

The calculated development of vertical midspan displacement (see w_c^M on Fig. 8a) is presented in Fig. 10a, b for Test 1 and Test 2 separately. The demonstration of midspan displacement is adopted from Bailey and Lennon (2008), where the horizontal axis takes values of temperatures in fire compartment, while calculated or measured displacement is applied on the vertical axis. The displacements are computed for all three analysed temperature fields, i.e. S1, S2 and S3.

Figure 11 presents the development of midspan displacement w_c^M with time. It is discovered that the development of displacement w_c^M in the heating phase (up to 52 min in Test 1 and 62 min in Test 2, see Fig. 5) is almost identical for all three analysed cases (S1, S2 and S3). The result is expected, considering the fact, that calculated temperatures for all three cases were very similar (see Fig. 7). The calculated displacement in the heating phase also agree relatively well to the measured one, especially for the Test 2.

In the cooling phase of fire compartment, the calculated displacement coincide best for case S1 and fire development according to Test 2. In this case the maximum computed displacement $w_{c,max}^M = 418$ mm is achieved at time $t = 98$ min (see Figs. 10b or 11b). For the results when Test 1 is embedded, the maximum displacement $w_{c,max}^M = 353$ mm is calculated at time $t = 82$ min (see Figs. 10a or 11a). When constant temperature inside opening is considered, i.e. $T_0 = 20°C$ (case S2), the displacement in the cooling phase is in average 15% smaller. The reason for this lays in faster cooling due to the increased heat flux throughout the opening compared to the case S1. Computational failure in the cooling phase occurs only in the S3 study (for both Test 1 and Test 2). In this case the opening is isolated and the cooling of the HC slab has a considerably slower rate. The failure is a consequence of high tensile stresses in tendon at the HC slab midspan, that reach tensile strength of prestressing steel. This is well observed in Fig. 12, where the computed time development of normal stresses in tendon σ_p and compression stresses in concrete fiber σ_c in point C (see Fig. 8) at the HC slab midspan are demonstrated. The stresses are compared to the corresponding temperature dependent strengths of tendon $f_{py,T}$ and concrete $f_{c,T}$. The values are normalized.

In addition, time development of normal stresses in tendon and concrete fiber for case S1 are represented in Fig. 13. The observed location is the same, i.e the HC slab midspan and point C for concrete. As noticed, the computational failure does not take place. However, the stresses in tendon in the cooling phase are getting very close to the tensile strength of tendon, particularly for Test 2 (see Fig. 13b).

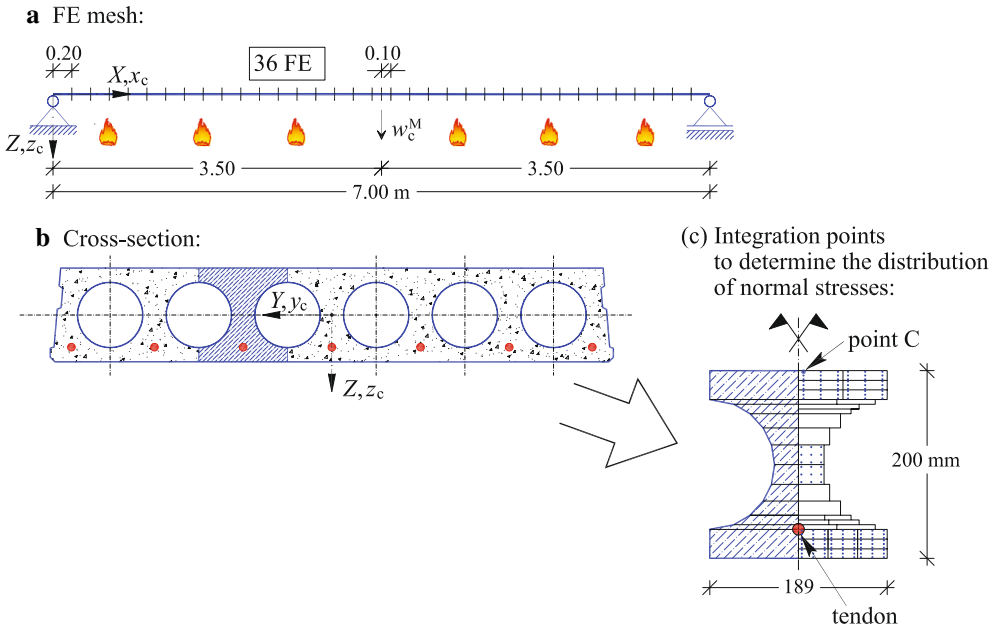

Fig. 8 FE mesh and distribution of integration points over the HC slab cross-section.

Based on the analyses, the most important conclusion is that the opening within the HC slab needs to be considered in case of natural fire, since it has a very important influence on temperature distributions over the HC slab cross-section in the cooling phase which eventually affects also the mechanical response of the HC slab.

4.2 Influence of Contact Stiffness Between Tendon and Concrete on the Mechanical Behaviour of the HC Slab During Fire

The presented numerical model allows to analyse stress–strain state of prestressed member taking into account the slip at the contact between tendon and concrete. Thus, the aim of parametric study is to analyse the influence of contact stiffness on the mechanical behaviour of the HC slab subjected to fire. The results of the analysis where slip was allowed (see Sect. 4.1.2) are compared with the result where fully stiff contact between tendon and concrete was considered. The other parameters remains the same. The considered fire scenario is according to Test 2, while temperature field was taken from case S1. Different outcomes of this parametric study are presented in Figs. 14, 15, and 16.

The contact stiffness does not have a significant impact on the development of midspan displacement w_c^M. There is a minimum discrepancy observed only in the cooling phase of fire compartment (see Fig. 14a). However, contact stiffness has a decisive role on the distribution

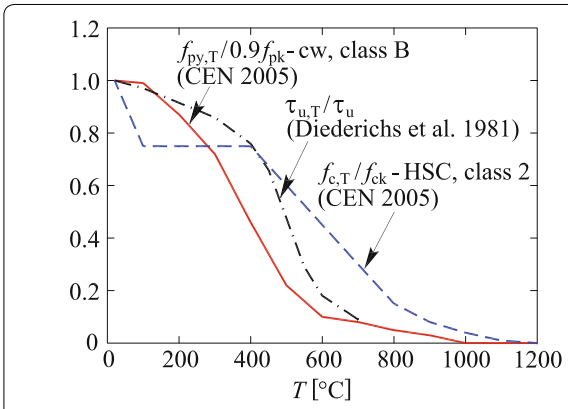

Fig. 9 The variations of strengths with temperatures.

of normal stresses σ_p at the HC slab ends (see Fig. 14b). When modelling fully stiff contact it is impossible to account the intake mechanism of prestressing force on the concrete section. Further on, it is also not possible to determine the distribution and development of slip Δ at the contact (see Fig. 14c) during fire, and consequently to evaluate the change of bond stresses τ at the contact (see Fig. 14d). Without this information it is difficult to assess the load bearing capacity of the contact and possible influence of contact failure on the mechanical repose of the HC slab during fire. In this study it is discovered that the maximum bond stress of the contact appear

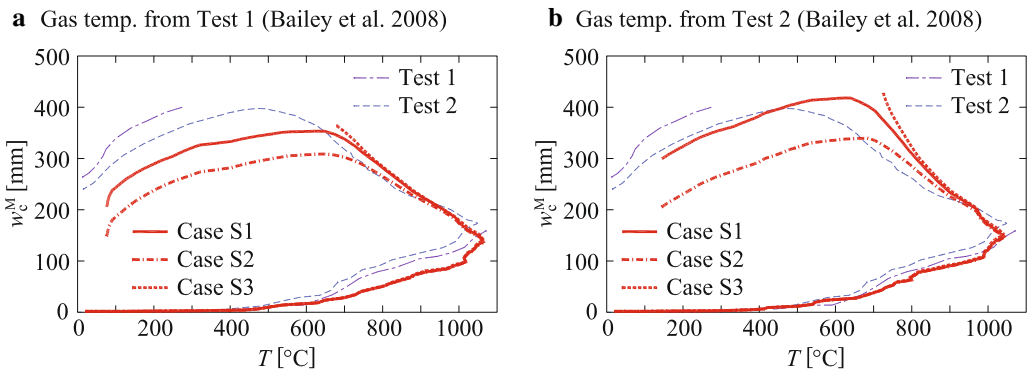

Fig. 10 Development of computed and measured vertical midspan displacements as a function of fire compartment temperature: **a** gas temperatures from Test 1 and **b** from Test 2.

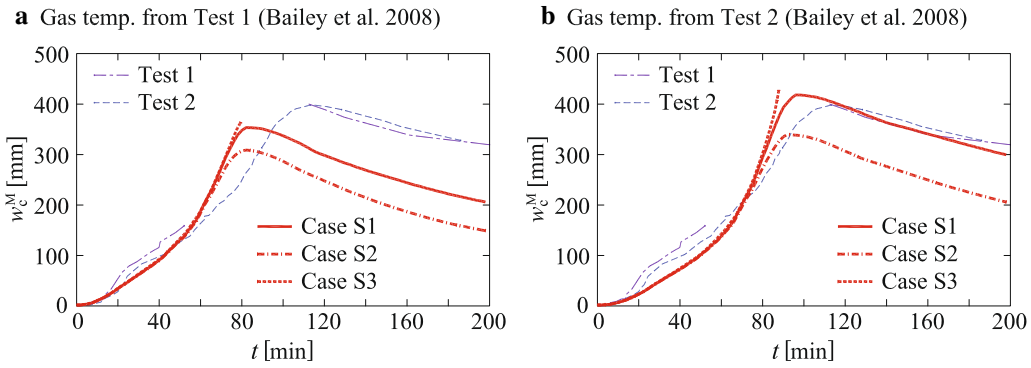

Fig. 11 Development of computed and measured vertical midspan displacements with time: **a** gas temperatures from Test 1 and **b** from Test 2.

exactly at the HC slab ends. Maximum bond stress prior fire occurrence takes values $\tau_{edge} = 5.41$ MPa (i.e. 99% τ_u) and reduces with higher simulation time. Simultaneously, the bond stresses as well as slips in the middle of the HC slab begin to increase due to the crack occurrence in concrete, and get a typical oscillating development (see Fig. 14c and d). Similarly was found in (Markovič et al. 2013; Rabczuk and Belytschko 2006). After 90 min of fire exposure the maximum bond stress at the HC slab ends is $\tau_{edge} = 3.29$ MPa, while in the middle it is 2.6 MPa. At this time, the corresponding bond strength at the beam ends is $\tau_{u,T} = 3.43$ MPa, meaning that the bond stress represent the 96% of the bond strength.

Increase of the bond stress at the tendon–concrete interface on certain part of beam's span is a result of concentration of cracks and strain localization as observed on Fig. 15a and b, where distribution of extensional strain and pseudo-curvature of the reference axis of the concrete part along the length of the beam is depicted. Due to the assumption of constant strain distribution over the length of the finite element somewhat stepwise distribution of strains on Fig. 15 can be observed.

Strain localization is also observed in the distribution of extensional strain in the tendon ε_p (see Fig. 16). This holds true also in case of rigid concrete-tendon contact, where extensional tendon strains are equal to extensional concrete strains at the position of tendon ($\varepsilon_p = \varepsilon_c$). It is further discovered, that in case of slip contact, the tendon strain at the HC slab ends is the same as temperature strain of tendon. This is s consequence of unloaded tendon at the HC slab ends and the assumption of additive decomposition of geometrical strain (see Sect. 2.2).

5 Conclusions

The paper presents a new two-phase numerical model to determine the response of the HC slab exposed to natural fire. In the first phase, own developed coupled hygro-thermo-chemical model was used. In addition, the impact of the opening within the HC slab geometry on temperature distribution across the concrete part of the HC slab was considered. In the second phase, the

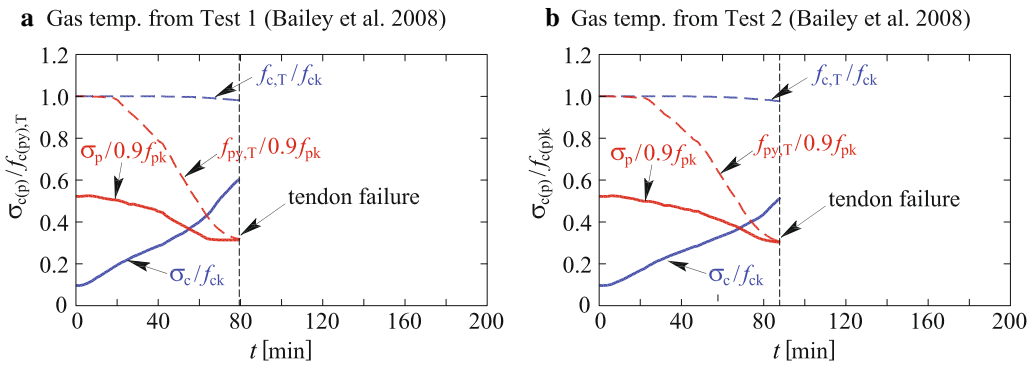

Fig. 12 Time development of normalized stresses in tendon and concrete (point C) at the HC slab midspan for case S3: **a** gas temperatures from Test 1 and **b** from Test 2.

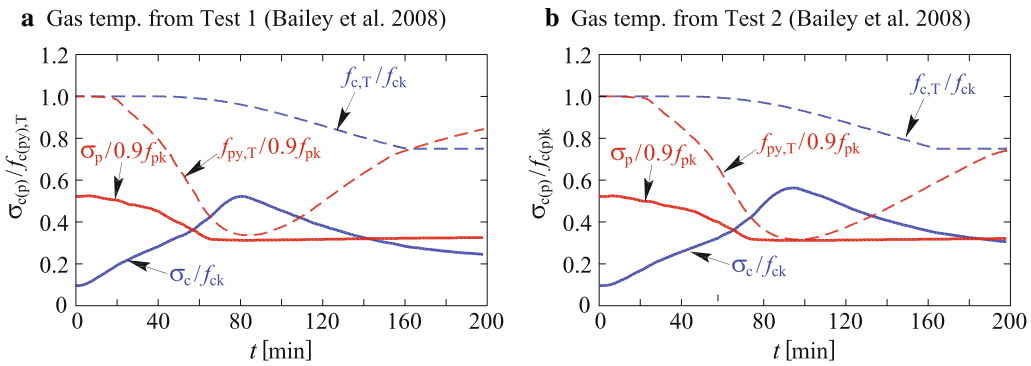

Fig. 13 Time development of normalized stresses in tendon and concrete (point C) at the HC slab midspan for case S1: **a** gas temperatures from Test 1 and **b** from Test 2.

new developed mechanical model was given, accounting for material and geometrical non-linearity as well as the slip between concrete and tendon. Based on the studies presented in the paper, the following conclusions can be given:

(i) geometrical opening in the HC slab had a minor impact on the temperature distribution in the heating phase. However, it had a considerable influence on the temperature distribution in the cooling phase, acting as an energy sink. When the opening was isolated (prevented heat and mass flux) much slower temperature decrease occurred in the cooling phase,

(ii) the opening did not have any impact on the development of midspan vertical displacement of the HC slab in the heating phase, while significant influence was observed in the cooling phase,

(iii) comparison of the calculated and measured temperatures (Bailey and Lennon 2008) revealed good agreement in the heating phase, whereas some discrepancies were found in the cooling phase. The reason for this may be attributed to the concrete cracking occurring in the experiment. The current hygro-thermo-chemical model does not allow to account for the influence of concrete cracking on the distribution of temperature and moisture within the concrete cross-section,

(iv) numerically determined time development of midspan displacement agreed well with the experimental results,

(v) considerable discrepancies between the numerical and the measured displacements were obtained in case S3, i.e., when the opening was isolated and, consequently, cooling rate of the HC slab was much slower. In this case, failure of the HC slab was noticed as a consequence of exceeded tensile stresses in tendon in the cooling phase.

(vi) the parametric study revealed that different contact stiffnesses between concrete and tendon (fully rigid or slip allowed) had minor influence on the development of midspan vertical displacement. However, consideration of the slip was decisive in the evaluation of bond stresses and load bearing capacity of the contact, meaning that the potential

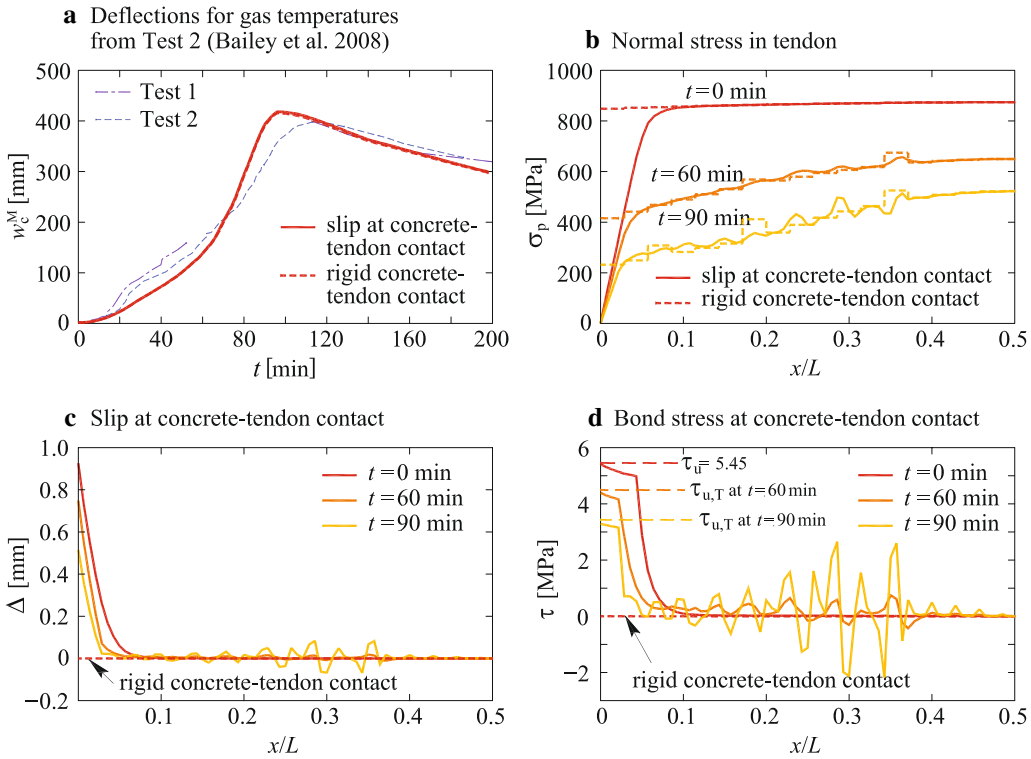

Fig. 14 The influence of different contact model (slip and rigid) on the development of chosen quantities.

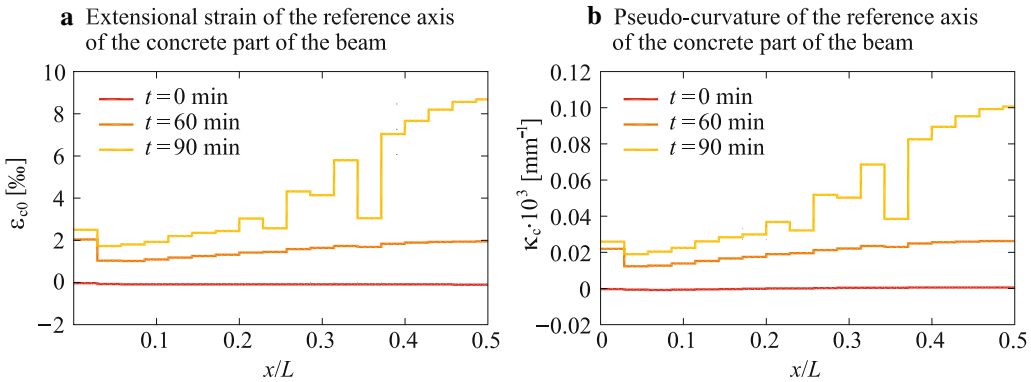

Fig. 15 The distributions of extensional strains and pseudo-curvature along the concrete part of the beam at different simulation times.

contact failure could be accounted for, which was not possible with the fully rigid connection. Thus, more realistic and more accurate behaviour of the HC slab in natural fire was possible.

Based on the performed validation and parametric studies it can be concluded that the newly presented two-phase numerical model is appropriate for the analysis of the HC slab exposed to natural fire and presents an important way towards performance-based approach.

Although the newly presented two-phase numerical model is based on a highly detailed physical description of the problem, some future work is still needed to fully generalize the model. Thus, further validation of the model for other natural fire curves is needed. Further on, the radiative heat transfer between the concrete and the opening is planned to be considered. With smaller adjustments of the boundary conditions, the post-tensioning can also be included in the model. The aim is also to develop fully coupled thermo-mechanical model in order to analyse the spalling of concrete.

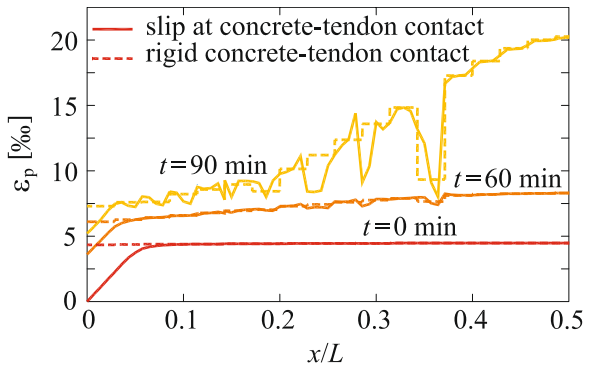

Fig. 16 The distributions of extensional strains in the tendon along the beam at different simulation times.

Acknowledgements
The authors acknowledge the financial support from the Slovenian Research Agency (research core Funding Nos. P2-0260 and P2-0158).

Authors' contributions
TH developed hygro-thermo-chemical model. IP and SB developed mechanical model for the response of prestressed concrete elements during fire. RP used both models and upgraded them to be applicable for the HC slab and to account for the phenomena occuring in the cooling phase. RP wrote the initial draft of manuscript, SB added additional parametric studies. TH and IP supervised and reviewed all the versions of the manuscript. All authors read and approved the final manuscript.

Funding
Not applicable.

Availability of data and materials
Not applicable

Competing interests
The authors declare that they have no competing interests.

Received: 21 May 2019 Accepted: 21 September 2019
Published online: 16 December 2019

References

Aguado, J., Espinos, A., Hospitaler, A., & Romero, M. (2012). Influence of reinforcement arrangement in flexural fire behavior of hollow core slabs. *Fire Safety Journal*, *53*, 72–84.
Aguado, J., Albero, V., Espinos, A., Hospitaler, A., & Romero, M. (2016). A 3D finite element model for predicting the fire behaviour of hollow-core slabs. *Engineering Structures*, *108*, 12–27.
Anderberg, Y., & Thelandersson, S. (1976). *Stress and deformation characteristics of concrete at high temperatures. Experimental investigation and material behaviour model*. Sweden: Lund Institute of Technology.
Bailey, C., & Lennon, T. (2008). Full-scale fire tests on hollowcore floors. *The Structural Engineer*, *86*, 33–39.
Bratina, S., Planinc, I., Saje, M., & Turk, G. (2003). Non-linear fire-resistance analysis of reinforced concrete beams. *Structural Engineering and Mechanics*, *16*, 695–712.
Bratina, S., Saje, M., & Planinc, I. (2004). Materially and geometrically non-linear analysis of reinforced concrete planar frames. *International Journal of Solids and Structures*, *41*, 7181–7207.
Bratina, S., Saje, M., & Planinc, I. (2007). The effects of different strain contributions on the response of RC beams in fire. *Engineering Structures*, *29*, 418–430.
CEN. (2004). Eurocode 1—action on structures—part 1-2: general actions—actions on structures exposed to fire. EN 1991-1-2, Brussels, Belgium
CEN. (2005). *EN 1992-1-2, Eurocode 2-Design of concrete structures—Part 1–2: General rules—Structural fire design*. Belgium: CEN.
Cengel, Y. A. (1998). *Heat transfer: A practical approach*. New York: WCB/McGraw-Hill.
Chang, J., Buchanan, A. H., Dhakal, R. P., & Moss, P. J. (2008). Hollow-core concrete slabs exposed to fire. *Fire and Materials*, *32*(6), 321–331.
Davie, C. T., Pearce, C. J., & Bićanić, N. (2006). Coupled heat and moisture transport in concrete at elevated temperatures-effects of capillary pressure and adsorbed water. *Numerical Heat Transfer*, *49*, 8.
Diederichs, U., & Schneider, U. (1981). Bond strength at high temperatures. *Magazine of Concrete Research*, *33*(115), 75–84.
Ellobody, E. (2014). Advanced analysis of prestressed hollow core concrete slabs exposed to different fires. *Advances in Structural Engineering*, *17*(9), 1281–1298.
Harmathy, T. (1967). A comprehensive creep model. *Journal of Basic Engineering*, *89*(3), 496–502.
Hozjan, T. (2009). Nonlinear analysis of composite planar structures exposed to fire. Doctoral Thesis (in Slovene). Ljubljana: University of Ljubljana, Faculty of Civil and Geodetic Engineering.
Hozjan, T., Saje, M., Srpčič, S., & Planinc, I. (2010). Fire analysis of steel-concrete composite beam with interlayer slip. *Computers & Structures*, *89*, 189–200.
Keuser, M., & Mehlhorn, G. (1983). Bond between prestressed steel and concrete—computer analysis using ADINA. *Computers & Structures*, *17*(5–6), 669–676.
Khalaf, J., & Huang, Z. (2016). Analysis of the bond behaviour between prestressed strands and concrete in fire. *Construction and Building Materials*, *128*, 12–23.
Kodur, V. K. R., & Shakya, A. M. (2014). Modeling the response of precast, prestressed concrete hollow-core slabs exposed to fire. *PCI Journal Paper*, *59*(3), 78–94.
Kolšek, J., Planinc, I., Saje, M., & Hozjan, T. (2014). The fire analysis of a steel-concrete side-plated beam. *Finite Elements in Analysis and Design*, *74*, 93–110.
Markovič, M., Krauberger, N., Saje, M., Planinc, I., & Bratina, S. (2013). Non-linear analysis of pre-tensioned concrete planar beams. *Engineering Structures*, *46*, 279–293.
Min, J. L., Moss, P. J., Dhakal, R. P., & Buchanan, A. H. (2010). *Modelling the fire resistance of prestressed concrete floors using multi-spring connection elements*. In: Proc., 8th international conference on structures in fire Sif '10.
Park, M. K., Lee, D. H., Han, S. J., & Kim, K. S. (2019). Web-shear capacity of thick precast prestressed hollow-core slab units produced by extrusion method. *International Journal of Concrete Structures and Materials*, *13*(1), 7.
Rabczuk, T., & Belytschko, T. (2006). Application of particle methods to static fracture of reinforced concrete structures. *International Journal of Fracture*, *137*, 19–49.
Reissner, E. (1972). On one-dimensional finite-strain beam theory: The plane problem. *Zeitschrift fur angewandte Mathematik und Physik*, *23*(5), 795–804.
Shakya, A. M., & Kodur, V. K. R. (2015). Response of precast prestressed concrete hollowcore slabs under fire conditions. *Engineering Structures*, *87*, 126–138.
Shakya, A. M., & Kodur, V. K. R. (2017). Modeling shear failure in precast prestressed concrete hollowcore slabs under fire conditions. *Journal of Structural Engineering*, *143*(9), 400–410.
Tufail, M., Shahzada, K., Gencturk, B., & Wei, J. (2017). Effect of elevated temperature on mechanical properties of limestone, quartzite and granite concrete. *International Journal of Concrete Structures and Materials*, *11*(1), 17–28.
Wei, Y., Zhang, L., Au, F., Li, J., & Tsang, N. (2016). Thermal creep and relaxation of prestressing steel. *Construction and Building Materials*, *128*, 118–127.

Publisher's Note